NeuroImage 215 (2020) 116827

Contents lists available at ScienceDirect

NeuroImage

journal homepage: www.elsevier.com/locate/neuroimage

A quantitative analysis of cell-specific contributions and the role of anesthetics to the neurovascular coupling

Sebastian Sten [a,b], Fredrik Elinder [c], Gunnar Cedersund [d,1], Maria Engström [a,b,*,1]

[a] Department of Health, Medicine and Caring Sciences, Linköping University, Linköping, Sweden
[b] Center for Medical Image Science and Visualization (CMIV), Linköping University, Linköping, Sweden
[c] Department of Biomedical and Clinical Sciences, Linköping University, Linköping, Sweden
[d] Department of Biomedical Engineering, Linköping University, Linköping, Sweden

ARTICLE INFO

Keywords:
Functional hyperemia
Mathematical modeling
Cerebral hemodynamics
Systems biology
Functional magnetic resonance imaging (fMRI)
Blood oxygen level dependent (BOLD) response

ABSTRACT

The neurovascular coupling (NVC) connects neuronal activity to hemodynamic responses in the brain. This connection is the basis for the interpretation of functional magnetic resonance imaging data. Despite the central role of this coupling, we lack detailed knowledge about cell-specific contributions and our knowledge about NVC is mainly based on animal experiments performed during anesthesia. Anesthetics are known to affect neuronal excitability, but how this affects the vessel diameters is not known. Due to the high complexity of NVC data, mathematical modeling is needed for a meaningful analysis. However, neither the relevant neuronal subtypes nor the effects of anesthetics are covered by current models. Here, we present a mathematical model including GABAergic interneurons and pyramidal neurons, as well as the effect of an anesthetic agent. The model is consistent with data from optogenetic experiments from both awake and anesthetized animals, and it correctly predicts data from experiments with different pharmacological modulators. The analysis suggests that no downstream anesthetic effects are necessary if one of the GABAergic interneuron signaling pathways include a Michaelis-Menten expression. This is the first example of a quantitative model that includes both the cell-specific contributions and the effect of an anesthetic agent on the NVC.

1. Introduction

The temporal and spatial connection between the brain's neuronal activity and its hemodynamic responses, the neurovascular coupling (NVC), is a central aspect of brain function. This connection is the result of a complex interplay between neuronal cells and blood vessels which affects the cerebral blood flow (CBF), the cerebral blood volume (CBV), and the cerebral metabolic rate of oxygen ($CMRO_2$). It is essential to understand the underlying mechanisms of NVC to fully interpret neuroimaging, such as functional magnetic resonance imaging (fMRI) (Ogawa et al., 1990), which use hemodynamic changes as a proxy for neural activity (Logothetis et al., 2001; Shmuel et al., 2006).

To search for neuronal correlates of the fMRI signal, researchers rely on animal experiments, which normally are performed under anesthesia. Unfortunately, the commonly used anesthetics have a broad effect on brain cells, including changes in neuronal excitability, vascular reactivity, cerebral metabolism, and other physiological processes (Masamoto and Kanno, 2012; Gao et al., 2017). The quantitative effects of these changes vary between different anesthetics, and those detailed variations remain unknown. Nevertheless, the majority of anesthetics exert their effect by direct action on ion channels, like the ionotropic γ-aminobutyric acid (GABA)-activated $GABA_A$ and *N*-methyl-*D*-aspartate (NMDA)-activated glutamate receptors, or different types of K^+ channels (Franks, 2008; Franks and Lieb, 1994) (Fig. 1A, upper arrow). However, how these effects propagate from altered ion-channel activities to other NVC aspects remain to be determined (Fig. 1A, lower arrow). This means that a precise and correct interpretation of the NVC and its alterations during anesthesia needs to be obtained for an exhaustive interpretation of fMRI data (Iadecola, 2017).

A basic chain of events, describing the NVC, in both awake and anesthetized animals, is slowly emerging. This chain of events (summarized in Fig. 1B) starts with the release of excitatory neurotransmitters, such as glutamate, and ends with the release of multiple vasoactive signaling molecules acting on pericytes and vascular smooth muscle cells

* Corresponding author. CMIV, Linköping University/US, 581 83, Linköping, Sweden.
E-mail address: maria.engstrom@liu.se (M. Engström).
[1] These authors contributed equally to this work.

https://doi.org/10.1016/j.neuroimage.2020.116827
Received 25 February 2020; Accepted 26 March 2020
Available online 11 April 2020
1053-8119/© 2020 The Author(s). Published by Elsevier Inc. This is an open access article under the CC BY license (http://creativecommons.org/licenses/by/4.0/).

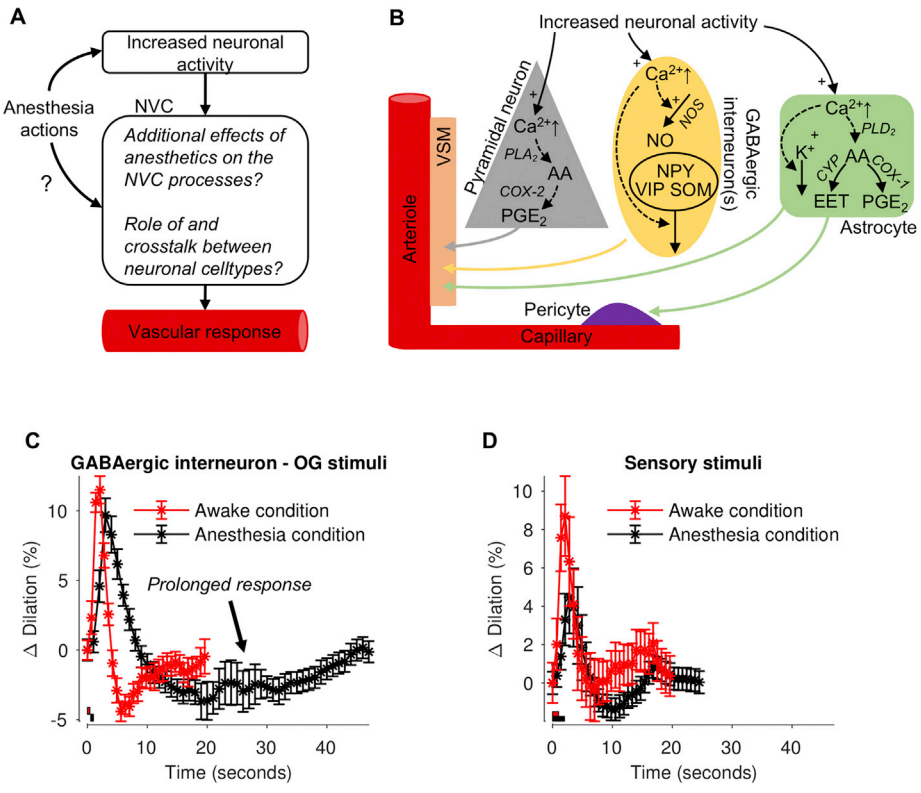

Fig. 1. A: Open questions regarding the NVC and the effects of anesthesia. **B: Simplified schematic illustration of the cellular pathways underlying the NVC.** Neuronal activity activates GABAergic interneurons (yellow oval), pyramidal neurons (grey triangle), and astrocytes (green rectangle), by stimulating influx of Ca^{2+}. Ca^{2+} acts as a second messenger, triggering signaling pathways in the different cells. In GABAergic interneurons, Ca^{2+} promotes nitric oxide (NO) through upregulation of nitric oxide synthase (NOS) as well as facilitating the release of different neuropeptides such as neuropeptide Y (NPY), vasoactive intestinal peptide (VIP), and somatostatin (SOM). In pyramidal neurons, Ca^{2+} promotes the synthesis of the arachidonic acid (AA) via phospholipase A2 (PLA_2), which in turn is metabolized to prostaglandin E2 (PGE_2) via cyclooxygenase-2 (COX-2). In astrocytes, arachidonic acid is synthesized via phospholipase D2 (PLD_2) and its metabolites PGE_2 and epoxyeicosatrienoic acid (EET) are synthesized via cyclooxygenase-1 (COX-1) and cytochrome P450 (CYP) epoxygenase, respectively. Furthermore, extracellular K^+ is increased upon neuronal activity. Together these vasoactive messengers act on arterioles and capillaries to modulate the vessel diameters, with the neuronal messengers acting primarily on the arterioles, and astrocytes acts on both arterioles and capillaries. **C & D: Characteristics of the arteriolar diameter responses extracted from** Uhlirova et al. (Uhlirova et al., 2016). Optogenetic (OG) (**C**) and sensory (**D**) stimuli-induced arteriolar diameter changes (y-axis) in awake and anesthetized animals (red and black symbols, respectively). The error bars depict the standard error of the mean (SEM). The bars in the lower left corner of each graph indicates the stimulus length for the OG light pulse of 450 ms (black) and 400 ms (red) and the sensory stimulation of 2 s (black) and 1 s (red) for awake and anesthetized animals, respectively.

(VSM) in the vessel walls (Attwell et al., 2010; Hillman, 2014). Activation of both excitatory and inhibitory neurons dilate cerebral vessels. More specifically, activation of excitatory pyramidal neurons release cyclooxygenase-2 (COX-2)-derived prostaglandin E2 (PGE_2), which in turn dilates arterioles (Lecrux et al., 2011; Lacroix et al., 2015) (Fig. 1B, grey triangle). Activation of inhibitory (*i.e.,* GABAergic) interneurons can release nitric oxide (NO), a potent vasodilator, and different vasoactive neuropeptides with both vasodilative (vasoactive intestinal peptide, VIP) or vasocontractile (neuropeptide Y, NPY; somatostatin) effects (Fig. 1B, yellow oval). The type of vasoactive molecules released depends on which type of the interneuron is activated (Markram et al., 2004; Cauli et al., 2004; Cauli and Hamel, 2010). In addition, astrocytes release arachidonic acid-derived messengers and K^+ ions, and affect CBF by acting on capillaries (Mishra et al., 2016) and arterioles (Filosa et al., 2006; Bazargani and Attwell, 2016; Mishra, 2017) (Fig. 1B, green rectangle). In summary, the NVC depends on a complex interplay between multiple cellular sources and targets, and the magnitude of each specific cellular contribution remains undetermined (Fig. 1A).

This complex interplay has been studied by the use of optogenetic (OG) stimulation, a technique where light-gated ion channels *e.g.*, channelrhodopsins, are expressed in the cellular plasma membrane and opened by exposure to light of a specific wavelength. In a recent OG study, Uhlirova et al. (2016), investigated the cell type-specific contributions to the NVC by selectively expressing channelrhodopsin-2 (ChR2) channels in either pyramidal neurons or GABAergic interneurons in mice. They measured arteriolar diameter changes *in vivo* upon both light-induced and sensory-induced stimulation in awake and anesthetized animals (Fig. 1C and D). They found that a light-induced activation of GABAergic interneurons evoked a biphasic (*i.e.,* an overshoot followed by a post-peak undershoot) hemodynamic response (Fig. 1C). Compared to awake condition (Fig. 1C, red symbols), anesthesia caused a prolonged response, lengthening the complete response by a factor of ~2.5 (Fig. 1C, black symbols). In contrast to these OG responses, sensory stimulation in awake or anesthetized animals evoked similar biphasic responses, with a larger post-peak undershoot in anesthetized animals (Fig. 1D, black and red symbols). In addition, Uhlirova and colleagues showed that NPY was responsible for the post-stimulus undershoot. This finding provides strong evidence for the active role of interneurons in facilitating and shaping the vascular response in the NVC. However, while such purely experimental research is essential, a quantitative systems-level understanding is still missing.

A quantitative systems-level understanding can be obtained using systems biology and mathematical modeling. A quantitative understanding is obtained if all remaining differences between simulations and experimental data can be viewed as measurement uncertainty (Cedersund and Roll, 2009; Cedersund, 2012). This stands in contrast to a qualitative understanding, which only requires that the qualitative features in experimental data – such as the presence of an overshoot or a post-peak undershoot – is captured by the simulations. Systems biology models provide a systems-level understanding if the models are based on biological mechanisms that together produce the model simulations. In other words, systems biology is not a statistical black-box method, but a method to formally test mechanistic hypotheses using experimental data (Cedersund and Roll, 2009). Previously, various modeling approaches have been used for NVC analysis: *e.g.,* multiple models describing phenomenological NVC mechanisms with a basis in fMRI (Buxton et al.,

1998; Mandeville et al., 1999; Vazquez et al., 2006; Havlicek et al., 2015; Kim et al., 2013; Kim and Ress, 2016) or optical imaging (Huppert et al., 2007, 2009). In recent years, mechanistic models, capturing the interplay between dilating and constrictive vasoactive substances produced as a result of intracellular signaling has gained traction (Yucel et al., 2009; Mathias et al., 2016, 2018; Lundengård et al., 2016; Sten et al., 2017). However, none of these models capture the precise mechanisms elucidated in Uhlirova et al. (2016). To our knowledge, no previous model has used OG data to either describe the interplay between GABAergic interneurons and pyramidal neurons in the NVC or their alterations during anesthesia.

Herein, we evaluate the experimental data presented in Uhlirova et al. (2016), using mechanistic systems biology modeling. We present a model capturing the mechanisms and interplay between GABAergic interneurons and pyramidal neurons with respect to data of arteriolar diameter changes (Fig. 2B). The model consists of three different levels: rapid neuronal activity, intracellular signaling pathways, and vascular responses. The model fits experimental data used for model training, featuring both awake and anesthetized animals. The model also correctly predicts experimental data not used for training, capturing the effect of different pharmacological inhibitors. In the model, the anesthetic agent acts on the rapid neuronal activity, and the OG-induced prolonged undershoot observed during anesthesia (Fig. 1C) can be explained if the vasoconstrictive effect of NPY follows Michaelis-Menten kinetics. In summary, our model provides a first example of a quantitative systems-level understanding of the cell-specific contributions to the NVC

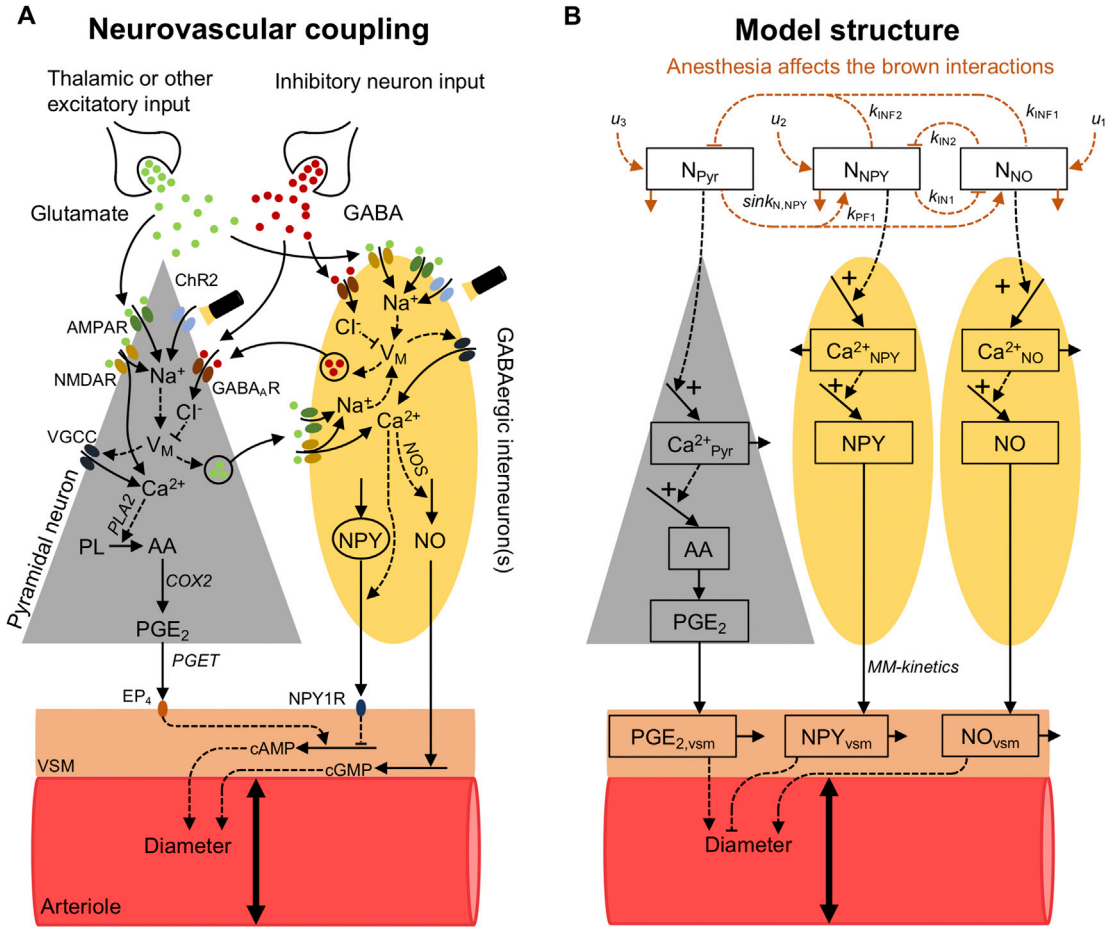

Fig. 2. Representation of the neurovascular system (A) and the model interaction graph (B). A: Two distinct types of cells are described: Pyramidal neurons (grey triangle, left) and GABAergic interneurons (further divided into NO-positive and NPY-positive; yellow oval shape, right). In pyramidal neurons, glutamate activates N-methyl-D-aspartate receptors (NMDAR) and α-amino-3-hydroxy-5-methyl-4-isoxazolepropionic receptors (AMPAR), resulting in an influx of Na^+ and Ca^{2+} ions, which lead to depolarization. γ-aminobutyric acid (GABA) activates $GABA_A$ receptors ($GABA_AR$) which prevents depolarization, thus counteracting the effect of glutamate. This balance between GABA and glutamate affect the membrane potential (V_M). Additionally, expressing a channelrhodopsin-2 (ChR2) ion channel in the cellular membrane allows for light-induced depolarization. Depolarization of a neuron opens voltage-gated calcium channels (VGCC), causing an additional influx of Ca^{2+} ions. In pyramidal neurons, Ca^{2+} activates phospholipase A2 (PLA2) which converts phospholipids (PL) into arachidonic acid (AA). In turn, AA is metabolized into prostaglandin E2 (PGE_2) by cyclooxygenase-2 (COX-2). Pyramidal neurons release glutamate during depolarization, which activate GABAergic interneurons through NMDAR and AMPAR activation. GABAergic interneurons release GABA when depolarized, inhibiting surrounding cells. In specific subtypes of GABAergic interneurons, Ca^{2+} ions activate nitric oxide synthase (NOS) which triggers the production and subsequent release of nitric oxide (NO). Other subtypes of GABAergic interneurons synthetize and express vesicle-bound vasoactive peptides such as neuropeptide Y (NPY). The release of these peptides is facilitated by Ca^{2+} ions. Vascular smooth muscle (VSM) cells (brown rectangle) enwrap arterioles (red cylinder) and regulates the arteriolar diameter. PGE_2 are transported over cellular membranes by prostaglandin E2 transporters (PGET) and promotes arteriolar dilation by relaxing VSM by activation of the prostaglandin EP_4 receptor and upregulation of cyclic adenosine monophosphate (cAMP) synthesis. NO diffuse freely over cellular membranes, and acts to increase the production of cyclic guanosine monophosphate (cGMP), which in turn promotes relaxation of VSM and arteriolar dilation. Lastly, NPY activates the G-protein coupled NPY Y1 receptor (NPY1R) expressed on VSM cells, which inhibits synthesis and thereby promote arteriolar constriction. **B:** Each box represents a state, while non-boxes represent variables. Mass-action kinetics are shown with fully drawn arrows, while non-mass action kinetics are shown in dashed lines. u_1, u_2, u_3 denotes the input signals used in the experimental setup. NPY_{vsm} and NO_{vsm} represents the effect of NPY and NO on the vascular smooth muscle cells. For the model evaluation, we postulate that the effect of the anesthetic can be replicated solely by altering the neuronal dynamics and input signal (brown arrows).

including their alterations by an anesthetic agent.

2. Methods

2.1. Model formulation

All models are formulated using ordinary differential equations (ODEs). The general notation of an ODE model is as follows:

$$\dot{x} = f(x, p, u, t) \tag{1a}$$

$$x(t_0) = x_0(p) \tag{1b}$$

$$\hat{y} = g(x, p, u, t) \tag{1c}$$

in which x is the vector of state variables, describing the concentration or amount of various substances, with respect to time; $\dot{x}$ represents the derivative of the states with respect to time; f and g are non-linear smooth functions; p is the vector of unknown constant parameters, here kinetic rate constants or scaling parameters; where u is the input signal corresponding to experimental data; where $x(t_0)$ contains the values of the states at the initial time point $t = t_0$, which are dependent on the parameters $x_0(p)$; and where $\hat{y}$ are the simulated model outputs corresponding to the measured experimental signal, here the arteriolar diameter change. Note that x, u, and $\hat{y}$ depend on t, but that the notation is dropped unless the time-dependence needs to be especially stated, as in Eq. (1b).

2.2. Model structure

In Fig. 2A, we present an NVC pathway. This pathway was simplified in the model, with a corresponding model interaction graph depicted in Fig. 2B. The interaction graph describes all of the reactions and interactions of the model. The stimulus u is given by the following equation

$$\mathrm{u}_i(t) = \begin{cases} 1 & t_{\mathrm{on}} \le t \le t_{\mathrm{off}} \\ 0 & \text{otherwise} \end{cases} \tag{2}$$

where t_{on}, t_{off} are the times when the signal goes on and off, respectively.

2.2.1. Presynaptic activity and calcium influx

Glutamate and GABA are released from different types of neurons and bind to specific ion channel-coupled receptors located in the plasma membrane of post-synaptic neurons. The primary excitatory neurotransmitter, glutamate, bind to NMDA and α-amino-3-hydroxy-5-methyl-4-isoxazolepropionic acid (AMPA) receptors. Activation of these ion channel-coupled receptors open ion-conducting pores leading to an influx of Na^+ and Ca^{2+} ions, causing a depolarization of the neuron. This in turn opens voltage-gated calcium channels, allowing additional influx of Ca^{2+} ions. In contrast, GABA prevents depolarization of neurons by binding to the ion channel-coupled $GABA_A$ receptor, which opens Cl^- ion-conducting pores. Several general anesthetics, including α-chloralose used in Uhlirova et al. (2016), act as positive allosteric modulators on the $GABA_A$ receptor, potentiating the Cl^- ion conductance by increasing the affinity of GABA (Garrett and Gan, 1998).

Pyramidal neurons are glutamatergic, meaning that glutamate is released upon depolarization, and acts on *e.g.* astrocytes and interneurons. GABAergic interneurons release GABA upon depolarization and act on pyramidal neurons or other interneurons. This forms a canonical neuronal circuit, where interneurons play a key role in regulating the activity of pyramidal neurons. Glutamate acts to depolarize neurons and to increase the intracellular Ca^{2+} levels, while GABA acts to prevent neurons to depolarize. In the model, we represent these interplays between pyramidal and inhibitory interneuron activity and their effect on respective neuronal Ca^{2+} levels as

$$\frac{d\mathrm{N_{NO}}}{dt} = k_{\mathrm{u,NO}}\mathrm{u}_1 + k_{\mathrm{PF1}}E_{\mathrm{Pyr}} - k_{\mathrm{IN1}}E_{\mathrm{NPY}} - sink_{\mathrm{N,NO}}\mathrm{N_{NO}} \tag{3a}$$

$$\frac{d\mathrm{N_{NPY}}}{dt} = k_{\mathrm{u,NPY}}\mathrm{u}_2 + k_{\mathrm{PF2}}E_{\mathrm{Pyr}} - k_{\mathrm{IN2}}E_{\mathrm{NO}} - sink_{\mathrm{N,NPY}}\mathrm{N_{NPY}} \tag{3b}$$

$$\frac{d\mathrm{N_{Pyr}}}{dt} = k_{\mathrm{u,\ Pyr}}\mathrm{u}_3 - k_{\mathrm{INF1}}E_{\mathrm{NO}} - k_{\mathrm{INF2}}E_{\mathrm{NPY}} - sink_{\mathrm{N,Pyr}}\mathrm{N_{Pyr}} \tag{3c}$$

$$\frac{d\left[\mathrm{Ca_i^{2+}}\right]}{dt} = k_{\mathrm{Ca}}(1 + N_{\mathrm{i}}) - sink_{\mathrm{Ca,i}}\left[\mathrm{Ca_i^{2+}}\right] \tag{3d}$$

$$E_i = \begin{cases} N_{\mathrm{i}}, & N_{\mathrm{i}} \ge 0 \\ 0, & N_{\mathrm{i}} < 0 \end{cases} \tag{3e}$$

Where $\mathrm{N_{NO}}$, $\mathrm{N_{NPY}}$, and $\mathrm{N_{Pyr}}$ describe the neuronal activity of the GABAergic NO and NPY interneurons, and the pyramidal neurons, respectively; $\mathrm{Ca_i^{2+}}$ represents intracellular calcium in respective neuron; $k_{\mathrm{u,i}}$ is the input strength of the stimulation to respective neuron; k_{PF1} and k_{PF2} are the kinetic rate parameters governing pyramidal to GABAergic interneuron signaling; k_{INF1} and k_{INF2} are the kinetic rate parameters describing the negative feedback from GABAergic interneurons to pyramidal neurons; k_{IN1} and $k_{\mathrm{IN2\ are}}$ the kinetic rate parameters describing the negative feedback between GABAergic interneurons; $sink_{\mathrm{N,i}}$ are kinetic rate parameters governing the degradation of the activity of respective neuron; k_{Ca} is the basal inflow rate of Ca^{2+} ($k_{\mathrm{Ca}} = 10$ for all three neurons); $sink_{\mathrm{Ca,i}}$ is the elimination rate of intracellular Ca^{2+} and i = (Pyr, NO, NPY), denotes the three different neuron types. To ensure reasonable neuronal dynamics, we limited the values of some parameters: $sink_{\mathrm{Ca,i}}$, $sink_{\mathrm{N,i}} > 1.28\ s^{-1}$ in line with experimental observations by (Majewska et al., 2000).

2.2.2. Pyramidal neuron signaling

The rise in intracellular Ca^{2+} levels in pyramidal neurons activates phospholipase A2 (PLA2) which leads, after some enzymatic steps, to an increase in intracellular arachidonic acid (AA) (Lacroix et al., 2015; Davis et al., 2004; Iadecola, 2017). This is described by the following equation

$$\frac{d[\mathrm{AA}]}{dt} = k_{\mathrm{PL}}\left[\mathrm{Ca_{Pyr}^{2+}}\right] - k_{\mathrm{COX}}[\mathrm{AA}] \tag{4}$$

where k_{PL} and k_{COX} are kinetic rate parameters. In pyramidal cells, AA is metabolized into PGE_2 through a COX-2 and PGE synthase rate-limiting reaction (Lecrux et al., 2011; Lacroix et al., 2015). PGE_2 promotes vasodilation by relaxing VSM cells and pericytes through activation of EP2 and EP4 receptors (Lacroix et al., 2015; Davis et al., 2004). In the model, this process is represented as

$$\frac{d[\mathrm{PGE_2}]}{dt} = k_{\mathrm{COX}}[\mathrm{AA}] - k_{\mathrm{PGE2}}[\mathrm{PGE_2}] \tag{5a}$$

$$\frac{d[\mathrm{PGE_{2,\ vsm}}]}{dt} = k_{\mathrm{PGE2}}[\mathrm{PGE_2}] - sink_{\mathrm{PGE2}}[\mathrm{PGE_{2,vsm}}] \tag{5b}$$

Where $\mathrm{PGE_{2,\ vsm}}$ represents PGE_2 acting on the VSM cells; $k_{\mathrm{PGE2\ and}}$ $sink_{\mathrm{PGE2}}$ are kinetic rate parameters.

2.2.3. GABAergic interneuron signaling

The rise in intracellular Ca^{2+} levels in GABAergic interneurons provoke the release of different vasoactive messengers. For instance, NO has previously been shown to be a potent vasodilator at the level of arterioles in both cortical slices and *in vivo* (Cauli et al., 2004; Mishra et al., 2016; Rancillac et al., 2006; Taniguchi, 2014). NO is released by specific NO-interneurons through a Ca^{2+} dependent nitric oxide synthase (NOS) rate limiting reaction. Here, we represent this process as

$$\frac{d[\mathrm{NO}]}{dt} = k_{\mathrm{NOS}}\left[\mathrm{Ca}^{2+}_{\mathrm{NO}}\right] - k_{\mathrm{NO}}[\mathrm{NO}] \tag{6a}$$

$$\frac{d[\mathrm{NO}_{\mathrm{vsm}}]}{dt} = k_{\mathrm{NO}}[\mathrm{NO}] - sink_{\mathrm{NO}}[\mathrm{NO}_{\mathrm{vsm}}] \tag{6b}$$

Where $\mathrm{NO}_{\mathrm{vsm}}$ represents NO acting on the VSM cells; k_{NOS}, k_{NO} and $sink_{\mathrm{NO}}$ are kinetic rate parameters. Here, $sink_{\mathrm{NO}} > 1\ s^{-1}$ following experimental work by (Vaughn et al., 1998).

The vasoconstrictive messenger responsible for the post-stimulus undershoot was identified by Uhlirova et al. as NPY. NPY is released by specific NPY producing subtypes of GABAergic interneurons and has previously been shown to induce vasoconstriction of vessels in slice preparations (Cauli et al., 2004; Kocharyan et al., 2008) and *in vivo* (Uhlirova et al., 2016). NPY acts by binding to the NPY receptor Y1, a $G_{\alpha i}$-protein coupled receptor which is expressed in VSM cells enwrapping arteries and arterioles (Bao et al., 1997; Abounader et al., 1995, 1999). Activation of this receptor inhibits the synthesis of adenosine monophosphate (cAMP) and increase the intracellular Ca^{2+} through an inositol-1,4,5-trisphosphate receptor (IP3R) dependent release from the sarcoplasmic reticulum (Tan et al., 2018). These processes lead to VSM contraction and a subsequent arteriolar vasoconstriction. In the model, these mechanisms are represented as:

$$\frac{d[\mathrm{NPY}]}{dt} = k_{\mathrm{NPY}}\left[\mathrm{Ca}^{2+}_{\mathrm{NPY}}\right] - \underbrace{\frac{\mathrm{V}_{\max}[\mathrm{NPY}]}{K_{\mathrm{M}} + [\mathrm{NPY}]}}_{v1} \tag{7a}$$

$$\frac{d[\mathrm{NPY}_{\mathrm{vsm}}]}{dt} = \underbrace{\frac{\mathrm{V}_{\max}[\mathrm{NPY}]}{K_{\mathrm{M}} + [\mathrm{NPY}]}}_{v1} - sink_{\mathrm{NPY}}[\mathrm{NPY}_{\mathrm{vsm}}] \tag{7b}$$

Where $\mathrm{NPY}_{\mathrm{vsm}}$ represents NPY acting on the VSM cells; k_{NPY} and $sink_{\mathrm{NPY}}$ are kinetic rate parameters. The conversion between intracellular NPY and NPY in the VSM, $\mathrm{NPY}_{\mathrm{vsm}}$, is governed by Michaelis-Menten kinetics (see Eq.7a–b, $v1$) (Michaelis and Menten, 1913; Johnson and Goody, 2011), where K_{M} is the Michaelis constant (the concentration of the substrate at which half max reaction rate is achieved) and $\mathrm{V}_{\max}$ is the maximal reaction rate. Michaelis-Menten kinetics was assumed for this reaction because initial tests with simpler mass-action kinetics could not produce a satisfactory agreement to the experimental data. The interpretation of Michaelis-Menten kinetics is that when $[\mathrm{NPY}] \ll K_{\mathrm{M}}$ the reaction behaves like a first-order mass-action reaction, meaning that the reaction is linearly dependent on [NPY] ($\mathrm{V}_{\max}$NPY]). However, as [NPY] increases beyond K_{M}, $[\mathrm{NPY}] \gg K_{\mathrm{M}}$, the reaction behaves like a zero-order reaction, meaning that the reaction is independent of [NPY], and only depends on the maximal reaction rate $\mathrm{V}_{\max}$. In between these two limits, [NPY] has a saturated effect on the reaction rate and when [NPY] equals K_{M}, the reaction rate has reached half the maximum value.

2.2.4. Arteriolar diameter change

We express the arteriolar diameter as the per cent normalized weighted summation of the end states of the three vasoactive signaling pathways:

$$\begin{aligned} &\Delta D(\%) = 100 \cdot \frac{S(t) - S_0}{S_0} \\ &where:\ S = k_{y1}[\mathrm{NO}_{\mathrm{vsm}}(t)] + k_{y2}[\mathrm{PGE}_{2,\mathrm{vsm}}(t)] - k_{y3}[\mathrm{NPY}_{\mathrm{vsm}}(t)] \\ &S_0 = k_{y1}[\mathrm{NO}_{\mathrm{vsm}}(0)] + k_{y2}[\mathrm{PGE}_{2,\mathrm{vsm}}(0)] - k_{y3}[\mathrm{NPY}_{\mathrm{vsm}}(0)] \end{aligned} \tag{8}$$

Where k_{y1}, k_{y2}, k_{y3} are unknown weighting factors which determines the influence of each respective vasoactive pathway on the smooth muscle cells surrounding the arterioles.

2.3. Model evaluation

Once the model structure has been formulated (Fig. 2B) and data has been collected, the parameters, p, need to be determined. This is commonly done by evaluating the negative log-likelihood function. Assuming independent, normally distributed additive measurement noise, the likelihood of observing data D given p is:

$$J(p) = -log(L(D|p)) = \frac{1}{2}\sum_{e=1}^{n_e}\sum_{o=1}^{n_o^e}\sum_{s=1}^{n_s^{e,o}}\left[\log\left(2\pi\left(\sigma_s^{e,o}\right)^2\right) + \left(\frac{y_s^{e,o} - \hat{y}_s^{e,o}(p)}{\sigma_s^{e,o}}\right)^2\right] \tag{9}$$

where n_e is the number of experiments; n_o^e is the number of observables per experiment; $n_s^{e,o}$ is the number of samples per observable per experiment; $\sigma_s^{e,o}$ is the measurement uncertainty of the data point; $y_s^{e,o}$ is the measured data point; $\hat{y}(p)$ is the corresponding simulated data point.

If the measurement noise $\sigma_s^{e,o}$ is known, $J(p)$ share the same optimal parameters with the least-squares function J_{lsq}:

$$J_{lsq}(p) = \sum_{e=1}^{n_e}\sum_{o=1}^{n_o^e}\sum_{s=1}^{n_s^{e,o}}\left(\frac{y_s^{e,o} - \hat{y}_s^{e,o}(p)}{\sigma_s^{e,o}}\right)^2 \tag{10}$$

The summation in Eq. (10) and Eq. (11) gives the squared and normalized residuals, indicating how far the simulations $\hat{y}_s^{e,o}(p)$ are from the data $y_s^{e,o}$. In practice, the parameters are determined by optimizing $J(p)$ over p and the optimal parameters $\hat{p}$ are given by

$$\hat{p} = \mathrm{argmin} J(p) \tag{11}$$

2.4. Experimental data

All experimental data were obtained from the study of Uhlirova et al. (2016), and no new data were acquired in our study. Specifically, arteriolar diameter responses measured using two-photon imaging were extracted from Figs. 5 and 6 in Uhlirova et al. (2016) using the online tool WebPlotDigitizer (Rohatgi). The original article state that all experimental procedures were performed in accordance with UCSD Institutional Animal Care and Use Committee guidelines. In brief, four different stimulation protocols were used in their study: three conducted under the administration of the anesthetic α-chloralose, and the fourth during awake condition. The time series from the original manuscript were shown with error bars depicting the standard error of the mean (SEM). Below, condensed descriptions of each stimulation protocol are presented, and we kindly refer the reader to the original publication for a complete detailed description. For the model training, we used all control conditions specified below, and for model validation we used the conditions with pharmacological applications.

2.4.1. OG stimulation of pyramidal neurons during anesthesia

Thy1-ChR2-YFP mice (n = 2 subjects), with ChR2 selectively expressed in layer 5 pyramidal cells, were imaged (28 measurement locations along 13 arterioles within 40–380 μm range) during OG stimulation (single light pulse lasting 50–80 ms) under both control conditions (Fig. 3J, black error bars) and under the influence of both the AMPA/kaniate receptor antagonist 6-cyano-7-nitroquinoxaline-2,3-dione (CNQX, 500 μM) and the NMDA receptor selective antagonist D-(-)-2-Amino-5-phosphonopentanoic acid (AP5, 200 μM) (Fig. 4F, black error bars). The responses were extracted from Fig. 5A in (Uhlirova et al., 2016) by sampling all error bars, resulting in a time resolution of 1 s between each data point. In the model, we simplified the stimulus by assuming a fixed length of 100 ms affecting the pyramidal neuron with a constant value (*i.e.* a continuous box-car function). The stimulus amplitude, $k_{\mathrm{u,\ Pyr}}$, was treated as a free parameter and was optimized to fit data.

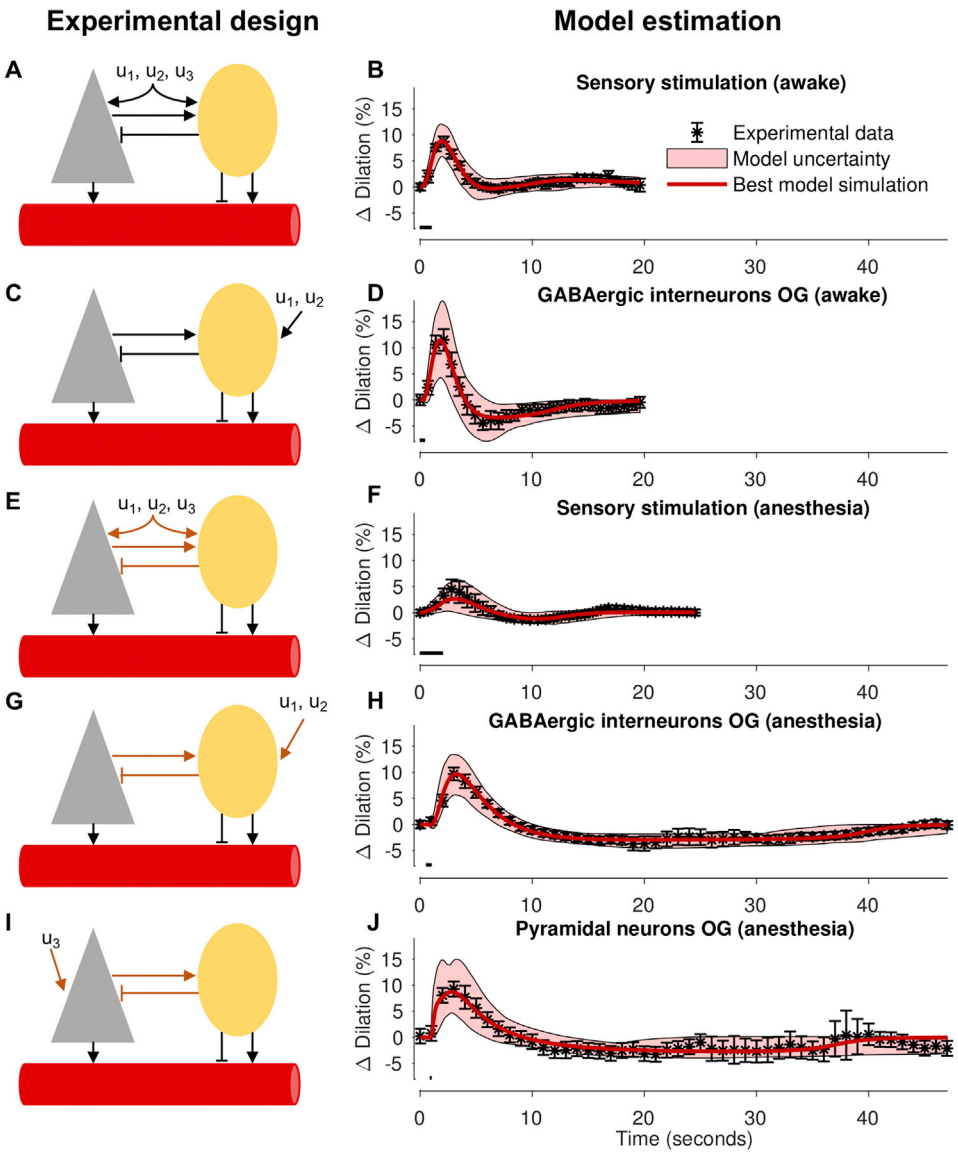

Fig. 3. Model evaluation to arteriolar response data from awake (A–D) and anesthetized animals (E–J) for both optogenetic (OG) (C–D, G–H, I–J) and sensory (A–B, E–F) stimuli. A, C, E, G; I: Simple schematics illustrating the experimental design for each data set. Grey triangle: pyramidal neuron; yellow circle: GABAergic interneurons. u_1, u_2, u_3 indicate the active inputs for each experimental setup (see Fig. 2B). **B, D, F, H, J:** Model estimation paired with experimental data. For each graph, best estimated model simulation (solid red line) paired with model uncertainty (red shaded areas) compared to experimental data (black symbols, error bars depicting standard error of the mean). The stimulation length is indicated by the black bar in the lower left portion of each graph.

2.4.2. OG stimulation of GABAergic interneurons during anesthesia

VGAT-ChR2(H134R)-EYFP mice (n = 3 subjects), with ChR2 selectively expressed in GABA interneurons, were imaged (52 measurement locations along 25 arterioles within 50–590 μm range) during OG stimulation (one pair of light pulses separated by 130 ms, for a total of 450 ms duration) under both control conditions (Fig. 3H, black error bars) and during application of the neuropeptide Y receptor Y1 inhibitor BIBP-3226 (100 μM) (Fig. 4D, black error bars). The responses were extracted from Fig. 5B in (Uhlirova et al., 2016) by sampling all error bars, resulting in a time resolution of 1 s between each data point. In the model, we assumed a constant stimulus value for the whole duration of 450 ms, scaled by the amplitude factors $k_{u,NPY}$ and $k_{u,NO}$ for respective neuron which were treated as free parameters.

2.4.3. Sensory stimulation during anesthesia

Additionally, 4 wild-type mice underwent imaging (10 measurement locations along 7 arterioles within 130–490 μm range) during sensory stimulation (2 s train of electrical pulses; train of six 100 μs, 1 mA delivered at 3 Hz) under both control conditions (Fig. 3F, black error bars) and during application of the neuropeptide Y receptor Y1 inhibitor BIBP-3226 (100 μM) (Fig. 4B, black error bars). The responses were extracted from Fig. 5C (left) in (Uhlirova et al., 2016) by sampling all error bars, resulting in a time resolution of 0.7 s between each data point. In the model, we assumed a constant stimulus value for the whole duration of 2 s, scaled by $k_{u,NPY}$, $k_{u,NO}$ and $k_{u,\ Pyr}$ affecting each respective neuron, and were treated as free parameters.

2.4.4. Sensory and OG stimulation during awake condition

Lastly, 4 wild-type and 3 VGAT-ChR2(H134R)-EYFP awake mice were imaged during sensory stimulation (1 s of air puffs, 100 ms puffs at 3 Hz) and OG stimulation (single light pulse lasting 150–400 ms), respectively (Fig. 3B and D, black error bars). The responses were extracted from Fig. 6A and B in (Uhlirova et al., 2016) by sampling all error bars, resulting in a time resolution of 0.7 s between each data point. In the model, we assumed a constant stimulus value for the whole duration scaled by the amplitude parameters $k_{u,i}$, with a length of 1 s and 400 ms for sensory and OG stimulation respectively.

Before being used in the model evaluation, SEM in all extracted time series with SEM measurements smaller than mean SEM was set to the mean SEM. This was done to avoid overfitting the model to a few extreme data points.

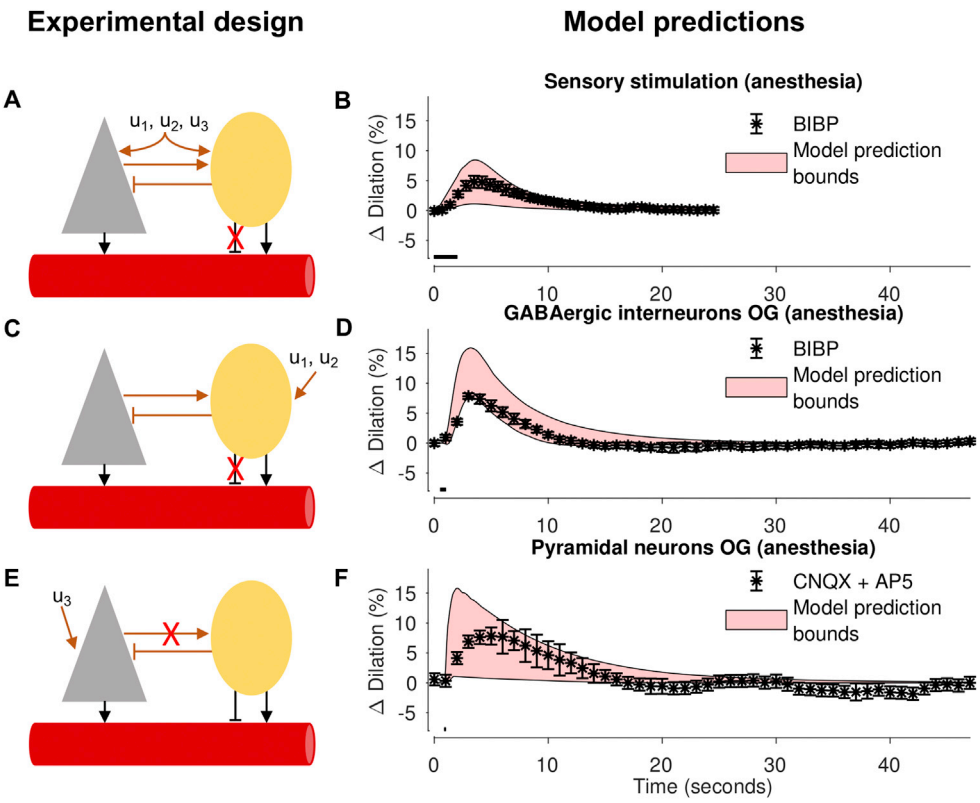

Fig. 4. Model predictions to drug perturbed arteriolar response data during anesthesia condition. Left: Simple schematics illustrating the experimental design for each data set. Yellow circle: GABAergic interneurons; Orange triangle: pyramidal neuron. u_1, u_2, u_3 indicate the active inputs for each experimental setup (see Fig. 2B). **Right:** Model predictions and experimental data. For each graph, model prediction uncertainty (red shaded areas) compared to experimental data (black symbols, error bars depicting standard error of the mean). The stimulus length is indicated by the black bar in the lower left portion of each graph. **A & B:** OG stimulation (400 ms) of GABAergic interneurons (B) and sensory stimulation (1 s) (C) during the presence of the NPY receptor Y1 antagonist BIBP. **C:** OG stimulation (100 ms) of pyramidal neurons in the presence of the glutamatergic signaling blockers AP5 and CNQX.

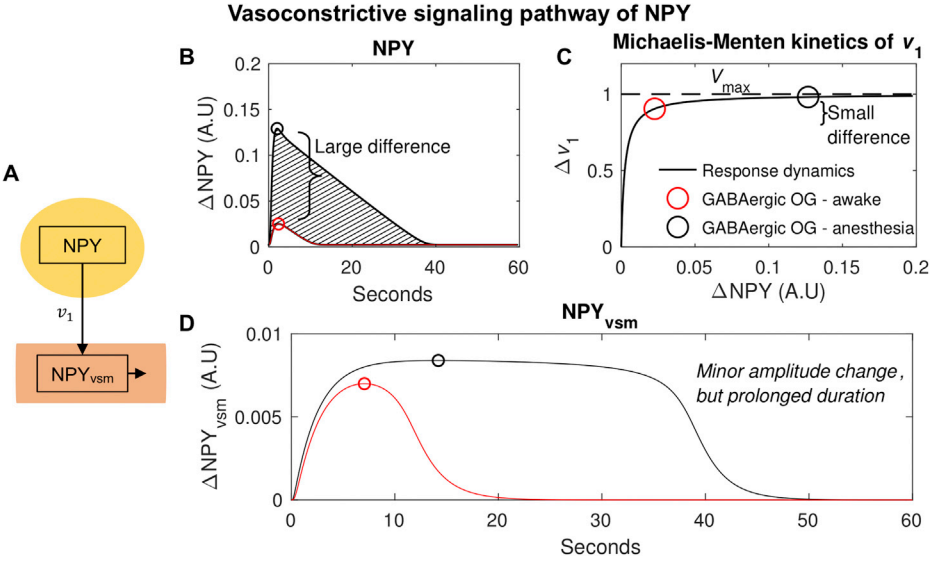

Fig. 5. Michaelis-Menten kinetics of NPY release can explain prolonged undershoot seen in experimental data. A: simple schematic of the NPY signaling arm governed by the Michaelis-Menten reaction v1 described in Eq. 7a–b. Note that we in the following simulations use the full model described in section 2.2 and Fig. 2B. **B:** simulation of [NPY] for GABAergic OG stimulation for awake (red solid line) and anesthetized (black solid line) animals. The difference between the responses are highlighted by the hatched area. **C:** reaction rate v_1 (y-axis, normalized to the maximal reaction rate V_{max}, black solid line) as a function of increasing [NPY] (x-axis). The achieved simulated maximal reaction rate for the different stimulus paradigms is shown in red (awake condition) and black (anesthesia condition) symbols. **D:** simulation of $[NPY_{vsm}]$ for GABAergic OG stimulation. For B & D, the change in respective state is shown on the y-axis, and time in seconds on the x-axis.

3. Results

3.1. Model hypothesis formulation

We created a new model structure specified by the equations in Section 2.2. In this model, the effects of the anesthetic appear solely for the rates affecting the neuronal dynamics (N_i, $i \in \{NO, NPY, Pyr\}$, see Eq. 3A-C). More specifically, we allow 12 parameters to change between awake and anesthetized animals: the three stimulus scaling parameters $k_{u,i}$ (Fig. 2B brown arrows); the three decay rate parameters $sink_{N,i}$ affecting N_i (Fig. 2B, solid brown arrows) and finally the six neuronal interaction parameters k_{PF1}, k_{PF2}, k_{IN1}, k_{IN2}, k_{INF1}, and k_{INF2} (Fig. 2B, dashed brown arrows). Furthermore, we allow the stimulus scaling parameters $k_{u,i}$ to change between OG and sensory stimulation. Further details on the model, estimation of parameter values, model analysis, and all simulation files to reproduce the results are available as Supplementary Materials.

3.2. The model can describe all experimental data used for model training, both qualitatively and quantitatively

The model was trained on experimental data consisting of all control responses from the Uhlirova et al. study (Uhlirova et al., 2016) (Fig. 3 right panel (B, D, F, H, J), black symbols). In Fig. 3 left panel (A, C, E, G,

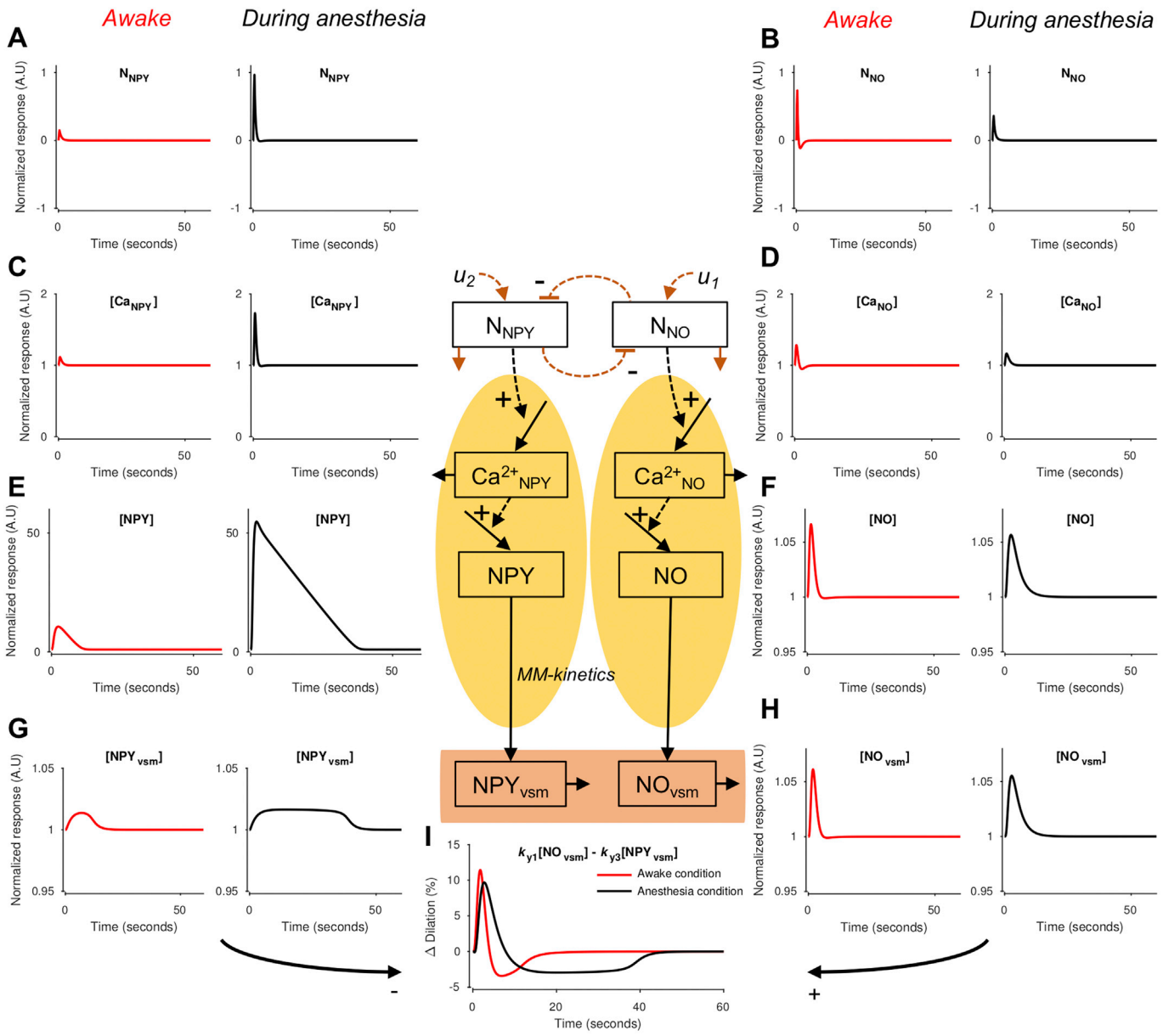

Fig. 6. Alterations in neuronal dynamics between awake and anesthetized animals in the case of optogenetic (OG) stimulation. The relevant states for a OG stimulation are depicted (see Fig. 2B for the complete model used for these simulations). The following states are displayed: the neuronal dynamics N_{NPY} (**A**) and N_{NO}(**B**); the calcium dynamics $[Ca_{NPY}]$ (**C**) and $[Ca_{NO}]$ (**D**); the first intracellular signaling state [NPY](**E**) and [NO](**F**); the vasoactive state of respective neuron, $[NPY_{vsm}]$ (**G**) and $[NO_{vsm}]$ (**H**), and finally, the resulting vascular response (**I**). For each of these states, two graphs are shown depicting the dynamics for awake (right (left graph, black solid line) and anesthetized (right graph, red solid line) animals. In the middle, an interaction graph showing how these states are connected, and which reaction that are altered with anesthesia (brown arrows) is shown. All time courses shown in the graphs are normalized to their baseline value for easier comparisons of the dynamics and amplitude between awake and anesthetized animals.

I), a simple schematic describes the experimental setup. The model parameters were fitted to the experimental data, achieving a qualitative and quantitatively acceptable fit (Fig. 3 right panel, solid thick red lines), evaluated using a χ^2-test ($J_{lsq}(\hat{p}_{H1}) = 42.4$, cut-off: χ^2 (190 data points) = 223.16 for $\alpha = 0.05$). Next, the uncertainty of the model was approximated using a Markov Chain Monte Carlo (MCMC) sampling algorithm. Posterior distributions of the parameters were sampled using 10^5 iterations. These distributions can be found in the supplementary material (Fig. S1) along with the point-wise parameter estimate. In addition, all χ^2 acceptable parameters ($J_{lsq}(p) < 223.16$) found during the MCMC sampling were saved. Using the generated Markov chains and acceptable χ^2 parameters, a confidence interval:

$$CI_\alpha = \left(p \middle| J_{lsq}(p) \leq J_{lsq}(\hat{p}) + \Delta_\alpha\left(\chi^2_{df}\right)\right) \tag{12}$$

was drawn where the threshold $\Delta_\alpha(\chi^2_{df})$ is the α quantile of the χ^2_{df} statistics (Kreutz et al., 2013; Maiwald et al., 2016). The significance was set to $\alpha = 0.05$ and degrees of freedom $df_{H1} = 46$, equal to the number of estimated parameters. The resulting uncertainty is depicted in the form of shaded red areas in Fig. 3, right panel.

As seen in Fig. 3 (right panel), the best model fits (solid red lines) lie within experimental uncertainty (black symbols) in all five experiments. In addition, all quantitatively acceptable model simulations (red shaded areas) follows the same dynamic behavior as seen in the data. These results mean that the model is capable of describing experimental data used for model training, both qualitatively and quantitatively.

3.3. The model can predict experimental data not used for training

To further evaluate the model, we used the previously generated Markov chains (see Section 3.1) to generate model predictions of experimental data not used for training. More specifically, all acceptable parameter sets within the confidence interval were used to predict the model response to a) sensory stimulation in the presence of NPY receptor Y1 antagonist BIBP (Fig. 4A and B); b) OG stimulation of GABAergic interneurons in the presence of the NPY receptor Y1 antagonist BIBP (Fig. 4C and D), and, c) OG stimulation of pyramidal neurons during inhibition of glutamatergic signaling by administration of the AMPA and NMDA antagonists CNQX and AP5, respectively (Fig. 4E and F). The corresponding experimental data used for these three pharmacological perturbations were extracted from Fig. 5 in Uhlirova et al. (2016). In the model, these inhibitions were carried out by: i) removing the transient effect of the NPY signaling arm on the arteriolar diameter change by setting $S = k_{y1}\mathrm{NO}_{\mathrm{vsm}}(t) + k_{y2}\mathrm{PGE}_{2,\mathrm{vsm}}(t) - k_{y3}\mathrm{NPY}_{\mathrm{vsm}}(0)$ (Fig. 4A–D), and, ii) removing feedback from pyramidal neurons to the GABAergic interneurons by setting $k_{\mathrm{PF1}} = k_{\mathrm{PF2}} = 0$, assuming a complete blockade of glutamatergic signaling (Fig. 4E and F).

Fig. 4 shows a simple illustration of each experimental setup (left panel, A, C, E) and model prediction uncertainties (B, D, F: red shaded areas) together with corresponding experimental data (black symbols). The model predictions follow the same qualitative behavior as the experimental data, overlapping the majority of all error bars. For Fig. 4A–D, we assume a complete inhibition of the transient NPY effect on arteriolar diameter, removing the possibility of negative deflection in arteriolar diameter change and thereby truncating the simulated responses to be positive for all timepoints (grey shaded areas). Finally, there are many of the individual curves within the uncertainty area that passes a χ^2-test, meaning that those predictions are also quantitatively correct.

3.4. The Michaelis-Menten kinetics of NPY signaling removes amplitude differences but preserves duration differences

Having established validity of the model, we now examine mechanistic properties of the system. The most prominent characteristic of the experimental data is the prolonged post-peak undershoot evoked by OG stimulation in anesthetized animals (Fig. 1C (black symbols); Fig. 3H–J) as compared to awake animals (Fig. 1C (red symbols); Fig. 3D). The key feature in the model producing this difference is the saturated signal propagation in the NPY signaling pathway, possible via the Michaelis-Menten expression (v_1 in Fig. 5A; see Eq. 7a–b, v_1). Upon OG stimulation, The increase of [NPY] is larger in anesthetized animals than awake (Fig. 5B, compare black and lines). This difference in [NPY] response disappears in the next reaction, which is the conversion of NPY to $\mathrm{NPY}_{\mathrm{vsm}}$ (governed by v_1), because [NPY] is above K_M, meaning that the reaction rate of v_1 has started to saturate (Fig. 5C). In other words, the increase from awake to anesthetized animals in [NPY] is large (>300% bigger; Fig. 5B), but the corresponding increase in v_1 is small (Fig. 5C, less than 20% bigger). This saturation implies that the dual difference between awake and anesthetized animals in [NPY] (Fig. 5B, higher amplitude and longer duration) is transformed to a basically single difference in $[\mathrm{NPY}_{\mathrm{vsm}}]$ (Fig. 5D, only longer duration).

This transformation is the key property in the NPY signaling leading to the prolonged post-peak undershoot when considered as a part of the entire system.

3.5. The model explains the prolonged post-peak undershoot in anesthesia conditions by a prolonged NPY signaling

To fully understand how the model explains the anesthesia-induced change in vascular dynamics, let us now consider the case of GABAergic OG stimulation for awake and anesthetized animals for the entire model. Fig. 6 shows the dynamics of the NPY and NO neurons, from the neuronal signaling to the release of their respective vasoactive agents. In the middle of the figure, a cut-out of the full interaction graph (Fig. 2B) is shown, highlighting the reactions changed between awake and anesthetized animals (Fig. 6, brown arrows).

Let us first follow the signal propagation in the left NPY branch (Fig. 6A, C, E, G). First, the anesthesia-induced changes (brown arrows) implies a difference in amplitude for the rapid neuronal response (Fig. 6A, $\mathrm{N}_{\mathrm{NPY}}$). This difference is then transformed to a difference in both amplitude and duration for the much longer [NPY] response (Fig. 6E).

Let us now follow the signal propagation in the right NO branch (Fig. 6B, D, F, H). As can be seen, there is here a smaller difference in amplitude, which stays relatively small throughout the entire signaling cascade.

Let us finally consider how these two branches combine to form the final response (Fig. 6I). The combined effect of the two branches is obtained by taking the difference between them: $[\mathrm{NPY}_{\mathrm{vsm}}]$ is vasoconstrictive and $[\mathrm{NO}_{\mathrm{vsm}}]$ is vasodilating. Since $[\mathrm{NO}_{\mathrm{vsm}}]$ is slightly lower in anesthesia, but with a preserved timing, and $[\mathrm{NPY}_{\mathrm{vsm}}]$ has a longer duration but roughly the same amplitude, the diameter dynamics has an approximately the same peak amplitude but a longer post-peak undershoot.

This simple analysis illustrates how straightforward model simulations can help unravel the mechanism by which our validated model explains the various facets of data.

4. Discussion

A model-based approach is necessary to fully understand the complexity of the NVC, but no previously existing model describes neither the relevant neuronal subtypes nor the effects of anesthetics (Fig. 1A). Herein, we provide a first systems biology model for the crosstalk between different GABAergic interneurons and pyramidal neurons. The model can quantitatively explain experimental data used for model training (Fig. 3) and correctly predict experimental data not used for training (Fig. 4), both for awake (Fig. 3A–D) and anesthetized (Fig. 3E–J; Fig. 4A–F) animals. The analysis shows that the prolonged post-peak undershoot in anesthesia can be explained solely by excitability changes since amplitude changes can be translated to downstream signal duration changes via a Michaelis-Menten expression (Figs. 5 and 6).

4.1. Previous models of the NVC

Numerous earlier studies have done mathematical modeling of arteriolar diameter changes e.g., convection-diffusion models based on: 1) transient blood oxygen level dependent (BOLD) signals (Kim et al., 2013; Kim and Ress, 2016; Zheng et al., 2005), 2) two-photon optical measurements (Huppert et al., 2007, 2009) or, 3) direct measurement of arteriolar diameter in mice (Barrett et al., 2012). Recently, spatio-temporal models such as vascular anatomical network (VAN) models (Fang et al., 2008; Boas et al., 2008; Gould et al., 2017) were shown capable of simulating the entire vascular network using two-photon imaging data and associated BOLD responses (Gagnon et al., 2015). However, these models do not include any biochemical mechanisms governing the intracellular processes underlying vasodilation and vasoconstriction. Some models exist which include such processes (Yucel et al., 2009; Mathias et al., 2016, 2018; Dormanns et al., 2015; Blanchard et al., 2016), but none of these models describe the molecular mechanism of NPY elucidated in Uhlirova et al. (2016); the difference between sensory and OG stimulation; the crosstalk between GABAergic interneurons and pyramidal neurons; or the effects of anesthetics.

4.2. The role of anesthetics in modulating the NVC

Previous experimental research has characterized different anesthetics and their effects on evoked hemodynamic responses, for instance

by looking at changes in response dynamics. Multiple studies have shown that 1) the amplitude of the evoked hemodynamic response (BOLD, CBV, CBF) are suppressed during anesthesia (Peeters et al., 2001; Martin et al., 2006; Goense and Logothetis, 2008; Pisauro et al., 2013; Aksenov et al., 2015; Drew et al., 2011); 2) in some cases, the observed hemodynamic response is slightly delayed compared to awake condition (Martin et al., 2006; Pisauro et al., 2013), and, 3) anesthetics induce changes in large scale neuronal networks, as seen in functional connectivity (Williams et al., 2010; Paasonen et al., 2018). The used anesthetic in Uhlirova et al. (2016), α-chloralose, is commonly used in animal research on the NVC because it preserves a robust hemodynamic response to sensory stimulation (Lindauer et al., 1993; Ueki et al., 1992). Garrett and Gan (1998) has reported that α-chloralose potentiates the GABA-induced $GABA_A$ current by increasing the affinity of GABA, thereby acting as a positive allosteric modulator on the $GABA_A$ receptor complex. Other studies have shown that α-chloralose reduces baseline CBF values (Masamoto and Kanno, 2012), increases blood pH, and decreases heart rate (Low et al., 2016), which could affect the measured BOLD responses.

In the used experimental data (Fig 1C; Fig. 3D, H, J), a clear difference can be seen between awake and anesthetized animals. For OG stimulation, the response during the awake condition (Fig. 3D) exhibits a faster post-peak undershoot phase compared to the anesthesia condition (Fig. 3H). For the sensory stimulation, the post-peak undershoot is reduced in awake animals (Fig. 3B, F). These changes are driven either by changes in neural processing or changes in vascular reactivity, or both. In the model, we have assumed that the anesthetic only affects the neuronal processing, allowing the parameters which governs the rapid neuronal dynamics to change between awake and anesthetized animals (see section 3.1). This assumption is sufficient to explain the used experimental data. This is possible because amplitude changes on the GABAergic interneuron activities (N_{NPY}) is translated into first amplitude and duration changes (for [NPY]) and then into only duration changes for ν_1 and [NPY_{vsm}] via the Michaelis-Menten expression for ν_1 (Fig. 5; Fig. 6A, C, E, G). Since the GABAergic NO interneurons only display a slightly smaller amplitude (Fig. 6B, D, F, H), the effect of adding the two GABAergic interneuron contributions together is a slightly decreased dilation and a clearly prolonged post-peak undershoot (Fig. 6I). Importantly, our analysis does not rule out that the observed effects of the anesthetic could be due direct effects of anesthetics on the arteriolar VSM or other vascular segments, since this possibility was not investigated with the model. However, a recent study by Vanlandewijck et al. (2018) reports that arteriolar VSM lack $GABA_A$ receptors in mice.

4.3. Other mechanisms facilitating the neurovascular coupling

The astrocytic contributions to the NVC *in vivo* is still unclear. The end-feet of astrocytes envelope cortical blood vessels, making them a potential mediator of the NVC. Indeed, previous studies have shown that astrocytes respond to neuronal activity via activation of glutamate receptors $mGluR_1$ and $mGluR_5$, triggering a rise in intracellular Ca^{2+} concentration through an inositol-1,4,5-trisphosphate receptor (IP3R) mediated mechanism and culminates in the release of vasoactive gliotransmitters such as prostaglandins, epoxyeicosatrienoic acids, or K^+ ions (Bazargani and Attwell, 2016). However, this explanation has recently been challenged, as Sun et al. (2013) reported that adult human and mouse astrocytes lack expression of $mGluR_1$ and $mGluR_5$ and other studies have reported that IP3R knockout mice retain unaltered NVC *in vivo* (Bonder and McCarthy, 2014). A recent study by Mishra et al. (2016) however, provided evidence for a new mechanism, where exogenous release of ATP from post-synaptic neurons triggers astrocytic Ca^{2+} influx through the ATP receptor $P2X_1$ with a subsequent capillary dilation as a result of cyclooxygenase-1 mediated PGE_2 release.

A recent study by Longden et al. (2017) shows that extracellular K^+ released by neuronal activity opens inward-rectifier K^+ ($K_{IR}2.1$) channels in capillary endothelial cells, inducing retrograde hyperpolarization which rapidly propagates to upstream arterioles, causing arteriolar dilation. Following this, Rungta et al. (2018) report a complete spatio-temporal vascular response from juxta-capillaries back to the pial arteriole. They show that local synaptic activation triggers a synchronous Ca^{2+} drop in mural cells along the upstream vascular tree. However, the parenchymal and first order arterioles dilate rapidly, preceding capillary dilation. Together, these studies show that the hemodynamic response can be initiated at the capillary level, spreading quickly through electrical signals propagating upstream the vascular tree, but arterioles form the primary unit for the onset of vascular responses. In the model, we do not account for the mechanism of retrograde hyperpolarization, and instead describe the onset of arteriolar dilation as dependent on local vasoactive messengers.

4.4. Sensitivity analysis versus prediction and parameter uncertainties

A sensitivity analysis is typically done to examine the result of local variations around a single point in the parameter space. Since we do not have a uniquely determined parameter point, but rather a long list of acceptable parameter values, such a point-wise local analysis is of limited value. We therefore believe that a global approach, which considers all acceptable parameters and basically ignores non-acceptable parameters, is the most appropriate analysis. MCMC is such a global approach. We use MCMC both to provide an estimate of model uncertainty for predictions and the uncertainty of each individual parameter. This approximates a sensitivity analysis, as it quantifies the impact of parameter changes on predictions: this impact is seen by the shaded regions in connection to each model simulation (for instance, Fig. 3). These uncertainty ranges should be considered in combination with the uncertainty of each individual parameter, which is given by the parameter distributions in Figure S1. This analysis does not exactly translate to a parameter specific sensitivity analysis, but rather provides an overall assessment of the relationship between the uncertainties in parameters and predictions considered as a whole. Nevertheless, given a specific parameter, a wide distribution implies that the parameter has a low sensitivity, and a narrow distribution implies that the parameter has a high sensitivity (when allowing for compensations of the other parameters to maintain a good agreement with data).

4.5. Assumptions and limitations

The present study has a number of limitations. The model structure is built upon underlying assumptions limiting the strength and scope of the conclusions that can be drawn. Nevertheless, such assumptions are necessary in order to develop a comprehensible model. In the model, we assume a simple relationship between GABAergic interneurons and pyramidal cells, where pyramidal neurons excite the GABAergic interneurons, which in turn act to inhibit the pyramidal neuron in a phenomenological manner (Eq. (3)). Here, a possible extension would be to include Hodgkin-Huxley description of ion-channel kinetics (Hodgkin and Huxley, 1952), describing the activity of each respective neuron as fluctuations of the membrane potential arising from opening and closing of ion channels due to glutamatergic and GABAergic signaling. Furthermore, the observed effect of disinhibition, where GABAergic interneurons are inhibited leading to excitation is not included. Other parts of the model structure lacking physiological details are the action of VSM cells and vessel elasticity of the arterioles. These mechanisms are simply represented by intermediary states (e.g., Eq. (6b)) in our model, which do not accurately capture the mechanisms of smooth muscle contraction or relaxation. In addition, our model does not include spatial dimensions or structural information regarding the cortical vessels, captured in other models (Boas et al., 2008; Aquino et al., 2014). Lastly, throughout the model, the amount of each state is specified in arbitrary units, which means that we describe biological values such as concentrations, scaled by unknown scaling constants. Note that this implies that the model still can be used to predict and simulate key observations that are possible to observe in experimental data, for example, the response time, relative

amplitudes between different stimulation strengths, whether there is a post-peak undershoot, etc.

4.6. Conclusions

We have provided a first quantitative systems-level understanding of GABAergic interneurons and pyramidal neurons in the NVC, in awake and anesthetized animals, in response to both sensory and OG stimulations. The model can qualitatively predict the effect of different pharmacological inhibitors (Fig. 4), and explain a key characteristic seen in experimental data: the post-peak undershoot is prolonged during anesthesia (Figs. 5 and 6). This explanation shows how our quantitative systems-level model can be used to understand the mechanistic underpinnings of complicated experimental observations in the NVC.

Funding

(The journal requires that funding is visible on the cover page during the review process).

The author(s) disclosed receipt of the following financial support for the research, authorship, and/or publication of this article: SS and ME received funding from the Swedish Research Council (2014-6249) and Knut and Alice Wallenberg Foundation (KAW, 2013.0076). GC received funding from the Swedish Research Council (2018-05418, 2018-03319), CENIIT (15.09), Swedish Foundation for Strategic Research (ITM17-0245) and H2020 (PRECISE4Q 777107).

Authors' contributions

SS, FE, GC and ME designed and conceived the study. SS carried out the model formulation, data extraction, numerical simulations and analysis. SS wrote the draft. FE, GC and ME provided critical revisions and edited manuscript.

Declaration of competing interestCOI

The author(s) declared no potential conflicts of interest with respect to the research, authorship, and/or publication of this article.

Appendix A. Supplementary data

Supplementary data to this article can be found online at https://doi.org/10.1016/j.neuroimage.2020.116827.

References

Abounader, R., Villemure, J.G., Hamel, E., 1995. Characterization of neuropeptide Y (NPY) receptors in human cerebral arteries with selective agonists and the new Y1 antagonist BIBP 3226. Br. J. Pharmacol. 116, 2245–2250.
Abounader, R., Elhusseiny, A., Cohen, Z., et al., 1999. Expression of neuropeptide Y receptors mRNA and protein in human brain vessels and cerebromicrovascular cells in culture. J. Cerebr. Blood Flow Metabol. 19, 155–163.
Aksenov, D.P., Li, L., Miller, M.J., et al., 2015. Effects of anesthesia on BOLD signal and neuronal activity in the somatosensory cortex. J. Cerebr. Blood Flow Metabol. 35, 1819–1826.
Aquino, K.M., Robinson, P.A., Drysdale, P.M., 2014. Spatiotemporal hemodynamic response functions derived from physiology. J. Theor. Biol. 347, 118–136.
Attwell, D., Buchan, A.M., Charpak, S., et al., 2010. Glial and neuronal control of brain blood flow. Nature 468, 232–243.
Bao, L., Kopp, J., Zhang, X., et al., 1997. Localization of neuropeptide Y Y1 receptors in cerebral blood vessels. Proc. Natl. Acad. Sci. U. S. A. 94, 12661–12666.
Barrett, M.J.P., Tawhai, M.H., Suresh, V., 2012. Arteries dominate volume changes during brief functional hyperemia: evidence from mathematical modelling. Neuroimage 62, 482–492.
Bazargani, N., Attwell, D., 2016. Astrocyte calcium signaling: the third wave. Nat. Neurosci. 19, 182–189.
Blanchard, S., Saillet, S., Ivanov, A., et al., 2016. A new computational model for {Neuro-Glio-Vascular} coupling: astrocyte activation can explain cerebral blood flow nonlinear response to interictal events. PloS One 11, e0147292.
Boas, D.A., Jones, S.R., Devor, A., et al., 2008. A vascular anatomical network model of the spatio-temporal response to brain activation. Neuroimage 40, 1116–1129.
Bonder, D.E., McCarthy, K.D., 2014. Astrocytic Gq-GPCR-linked IP3R-dependent Ca2+ signaling does not mediate neurovascular coupling in mouse visual cortex in vivo. J. Neurosci. 34, 13139–13150.
Buxton, R.B., Wong, E.C., Frank, L.R., 1998. Dynamics of blood flow and oxygenation changes during brain activation: the balloon model. Magn. Reson. Med. 39, 855–864.
Cauli, B., Hamel, E., 2010. Revisiting the role of neurons in neurovascular coupling. Front. Neuroenergetics 2, 9.
Cauli, B., Tong, X.-K., Rancillac, A., et al., 2004. Cortical GABA interneurons in neurovascular coupling: relays for subcortical vasoactive pathways. J. Neurosci. 24, 8940–8949.
Cedersund, G., 2012. Conclusions via unique predictions obtained despite unidentifiability–new definitions and a general method. FEBS J. 279, 3513–3527.
Cedersund, G., Roll, J., 2009. Systems biology: model based evaluation and comparison of potential explanations for given biological data. FEBS J. 276, 903–922.
Davis, R.J., Murdoch, C.E., Ali, M., et al., 2004. EP4 prostanoid receptor-mediated vasodilatation of human middle cerebral arteries. Br. J. Pharmacol. 141, 580–585.
Dormanns, K., van Disseldorp, E.M., Brown, R.G., et al., 2015. Neurovascular coupling and the influence of luminal agonists via the endothelium, 364, 49–70.
Drew, P.J., Shih, A.Y., Kleinfeld, D., 2011. Fluctuating and sensory-induced vasodynamics in rodent cortex extend arteriole capacity. Proc. Natl. Acad. Sci. U. S. A. 108, 8473–8478.
Fang, Q., Sakadžić, S., Ruvinskaya, L., et al., 2008. Oxygen advection and diffusion in a three-dimensional vascular anatomical network. Optic Express 16, 17530–17541.
Filosa, J.A., Bonev, A.D., Straub, S.V., et al., 2006. Local potassium signaling couples neuronal activity to vasodilation in the brain. Nat. Neurosci. 9, 1397–1403.
Franks, N.P., 2008. General anaesthesia: from molecular targets to neuronal pathways of sleep and arousal. Nat. Rev. Neurosci. 9, 370–386.
Franks, N.P., Lieb, W.R., 1994. Molecular and cellular mechanisms of general anaesthesia. Nature 367, 607–614.
Gagnon, L., Sakadžić, S., Lesage, F., et al., 2015. Quantifying the microvascular origin of BOLD-fMRI from first principles with two-photon microscopy and an oxygen-sensitive nanoprobe. J. Neurosci. 35, 3663–3675.
Gao, Y.-R., Ma, Y., Zhang, Q., et al., 2017. Time to wake up: studying neurovascular coupling and brain-wide circuit function in the un-anesthetized animal. Neuroimage 153, 382–398.
Garrett, K.M., Gan, J., 1998. Enhancement of gamma-aminobutyric acidA receptor activity by alpha-chloralose. J. Pharmacol. Exp. Therapeut. 285, 680–686.
Goense, J.B.M., Logothetis, N.K., 2008. Neurophysiology of the BOLD fMRI signal in awake monkeys. Curr. Biol. 18, 631–640.
Gould, I.G., Tsai, P., Kleinfeld, D., et al., 2017. The capillary bed offers the largest hemodynamic resistance to the cortical blood supply. J. Cerebr. Blood Flow Metabol. 37, 52–68.
Havlicek, M., Roebroeck, A., Friston, K., et al., 2015. Physiologically informed dynamic causal modeling of {fMRI} data. Neuroimage 122, 355–372.
Hillman, E.M.C., 2014. Coupling mechanism and significance of the BOLD signal: a status report. Annu. Rev. Neurosci. 37, 161–181.
Hodgkin, A.L., Huxley, A.F., 1952. A quantitative description of membrane current and its application to conduction and excitation in nerve. J. Physiol. 117, 500–544.
Huppert, T.J., Allen, M.S., Benav, H., et al., 2007. A multicompartment vascular model for inferring baseline and functional changes in cerebral oxygen metabolism and arterial dilation. J. Cerebr. Blood Flow Metabol. 27, 1262–1279.
Huppert, T.J., Allen, M.S., Diamond, S.G., et al., 2009. Estimating cerebral oxygen metabolism from fMRI with a dynamic multicompartment Windkessel model. Hum. Brain Mapp. 30, 1548–1567.
Iadecola, C., 2017. The neurovascular unit coming of age: a journey through neurovascular coupling in health and disease. Neuron 96, 17–42.
Johnson, K.A., Goody, R.S., 2011. The original Michaelis constant: translation of the 1913 michaelis–menten paper. Biochemistry 50, 8264–8269.
Kim, J., Ress, D., 2016. Arterial impulse model for the {BOLD} response to brief neural activation. Neuroimage 124, 394–408.
Kim, J., Khan, R., Thompson, J.K., et al., 2013. Model of the transient neurovascular response based on prompt arterial dilation. J. Cereb. Blood Flow Metab. Off. J. Int. Soc. Cereb. Blood Flow Metab. 33, 1429–1439.
Kocharyan, A., Fernandes, P., Tong, X.-K., et al., 2008. Specific subtypes of cortical GABA interneurons contribute to the neurovascular coupling response to basal forebrain stimulation. J. Cerebr. Blood Flow Metabol. 28, 221–231.
Kreutz, C., Raue, A., Kaschek, D., et al., 2013. Profile likelihood in systems biology. FEBS J. 280, 2564–2571.
Lacroix, A., Toussay, X., Anenberg, E., et al., 2015. COX-2-Derived prostaglandin E2 produced by pyramidal neurons contributes to neurovascular coupling in the rodent cerebral cortex. J. Neurosci. 35, 11791–11810.
Lecrux, C., Toussay, X., Kocharyan, A., et al., 2011. Pyramidal neurons are 'neurogenic hubs' in the neurovascular coupling response to whisker stimulation. J. Neurosci. 31, 9836–9847.
Lindauer, U., Villringer, A., Dirnagl, U., 1993. Characterization of CBF response to somatosensory stimulation: model and influence of anesthetics. Am. J. Physiol. 264, H1223–H1228.
Logothetis, N.K., Pauls, J., Augath, M., et al., 2001. Neurophysiological investigation of the basis of the fMRI signal. Nature 412, 150–157.
Longden, T.A., Dabertrand, F., Koide, M., et al., 2017. Capillary K+-sensing initiates retrograde hyperpolarization to increase local cerebral blood flow. Nat. Neurosci. 20, 717–726.
Low, L.A., Bauer, L.C., Klaunberg, B.A., 2016. Comparing the effects of isoflurane and alpha chloralose upon mouse physiology. PloS One 11, e0154936.

Lundengård, K., Cedersund, G., Sten, S., et al., 2016. Mechanistic mathematical modeling tests hypotheses of the neurovascular coupling in fMRI. PLoS Comput. Biol. 12, e1004971.
Maiwald, T., Hass, H., Steiert, B., et al., 2016. Driving the model to its limit: profile likelihood based model reduction. PloS One 11, e0162366.
Majewska, A., Brown, E., Ross, J., et al., 2000. Mechanisms of calcium decay kinetics in hippocampal spines: role of spine calcium pumps and calcium diffusion through the spine neck in biochemical compartmentalization. J. Neurosci. 20, 1722–1734.
Mandeville, J.B., Marota, J.J., Ayata, C., et al., 1999. Evidence of a cerebrovascular postarteriole windkessel with delayed compliance. J. Cerebr. Blood Flow Metabol. 19, 679–689.
Markram, H., Toledo-Rodriguez, M., Wang, Y., et al., 2004. Interneurons of the neocortical inhibitory system. Nat. Rev. Neurosci. 5, 793–807.
Martin, C., Martindale, J., Berwick, J., et al., 2006. Investigating neural–hemodynamic coupling and the hemodynamic response function in the awake rat. Neuroimage 32, 33–48.
Masamoto, K., Kanno, I., 2012. Anesthesia and the quantitative evaluation of neurovascular coupling. J. Cerebr. Blood Flow Metabol. 32, 1233–1247.
Mathias, E.J., Plank, M.J., David, T., 2016. A model of neurovascular coupling and the BOLD response: part I. Comput. Methods Biomech. Biomed. Eng. 1–11.
Mathias, E.J., Kenny, A., Plank, M.J., et al., 2018. Integrated models of neurovascular coupling and BOLD signals: responses for varying neural activations. Neuroimage 174, 69–86.
Michaelis, L., Menten, M.L., 1913. Die Kinetik der Invertinwirkung. Biochem. Z. 49, 333–369.
Mishra, A., 2017. Binaural blood flow control by astrocytes: listening to synapses and the vasculature. J. Physiol. 595, 1885–1902.
Mishra, A., Reynolds, J.P., Chen, Y., et al., 2016. Astrocytes mediate neurovascular signaling to capillary pericytes but not to arterioles. Nat. Neurosci. 19, 1619–1627.
Ogawa, S., Lee, T.M., Kay, A.R., et al., 1990. Brain magnetic resonance imaging with contrast dependent on blood oxygenation. Proc. Natl. Acad. Sci. U.S.A. 87, 9868–9872.
Paasonen, J., Stenroos, P., Salo, R.A., et al., 2018. Functional connectivity under six anesthesia protocols and the awake condition in rat brain. Neuroimage 172, 9–20.
Peeters, R.R., Tindemans, I., De Schutter, E., et al., 2001. Comparing BOLD fMRI signal changes in the awake and anesthetized rat during electrical forepaw stimulation. Magn. Reson. Imaging 19, 821–826.
Pisauro, M.A., Dhruv, N.T., Carandini, M., et al., 2013. Fast hemodynamic responses in the visual cortex of the awake mouse. J. Neurosci. 33, 18343–18351.
Rancillac, A., Rossier, J., Guille, M., et al., 2006. Glutamatergic control of microvascular tone by distinct GABA neurons in the cerebellum. J. Neurosci. 26, 6997–7006.
Rohatgi, Ankit, April, 2019. WebPlotDigitizer. Version: 4.2, San Francisco, California, USA. https://automeris.io/WebPlotDigitizer.
Rungta, R.L., Chaigneau, E., Osmanski, B.-F., et al., 2018. Vascular compartmentalization of functional hyperemia from the synapse to the pia. Neuron 99, 362–375 e4.
Shmuel, A., Augath, M., Oeltermann, A., et al., 2006. Negative functional {MRI} response correlates with decreases in neuronal activity in monkey visual area V1. Nat. Neurosci. 9, 569–577.
Sten, S., Lundengård, K., Witt, S.T., et al., 2017. Neural inhibition can explain negative BOLD responses: a mechanistic modelling and fMRI study. Neuroimage 158, 219–231.
Sun, W., McConnell, E., Pare, J.-F., et al., 2013. Glutamate-dependent neuroglial calcium signaling differs between young and adult brain. Science 339, 197–200.
Tan, C.M.J., Green, P., Tapoulal, N., et al., 2018. The role of neuropeptide Y in cardiovascular health and disease. Front. Physiol. 9, 1281.
Taniguchi, H., 2014. Genetic dissection of GABAergic neural circuits in mouse neocortex. Front. Cell. Neurosci. 8, 8.
Ueki, M., Mies, G., Hossmann, K.A., 1992. Effect of alpha-chloralose, halothane, pentobarbital and nitrous oxide anesthesia on metabolic coupling in somatosensory cortex of rat. Acta Anaesthesiol. Scand. 36, 318–322.
Uhlirova, H., Kilic, K., Tian, P., et al., 2016. Cell type specificity of neurovascular coupling in cerebral cortex. eLife 5. https://doi.org/10.7554/eLife.14315. Epub ahead of print.
Vanlandewijck, M., He, L., Mäe, M.A., et al., 2018. A molecular atlas of cell types and zonation in the brain vasculature. Nature 554, 475–480.
Vaughn, M.W., Kuo, L., Liao, J.C., 1998. Effective diffusion distance of nitric oxide in the microcirculation. Am. J. Physiol. Circ. Physiol. 274, H1705–H1714.
Vazquez, A.L., Cohen, E.R., Gulani, V., et al., 2006. Vascular dynamics and BOLD fMRI: CBF level effects and analysis considerations. Neuroimage 32, 1642–1655.
Williams, K.A., Magnuson, M., Majeed, W., et al., 2010. Comparison of alpha-chloralose, medetomidine and isoflurane anesthesia for functional connectivity mapping in the rat. Magn. Reson. Imaging 28, 995–1003.
Yucel, M.A., Devor, A., Akin, A., et al., 2009. The possible role of CO(2) in producing A post-stimulus CBF and BOLD undershoot. Front. Neuroenergetics 1, 7.
Zheng, Y., Johnston, D., Berwick, J., et al., 2005. A three-compartment model of the hemodynamic response and oxygen delivery to brain. Neuroimage 28, 925–939.